

Low-Valent Manganese Atoms Stabilized on Ceria for Nitrous Oxide Synthesis

Ivan Surin, Zhenchen Tang, Julian Geiger, Suyash Damir, Henrik Eliasson, Mikhail Agrachev, Frank Krumeich, Sharon Mitchell, Vita A. Kondratenko, Evgenii V. Kondratenko, Gunnar Jeschke, Rolf Erni, Núria López, and Javier Pérez-Ramírez*

Nitrous oxide, N_2O , exhibits unique reactivity in oxidation catalysis, but the high manufacturing costs limit its prospective uses. Direct oxidation of ammonia, NH_3 , to N_2O can ameliorate this issue but its implementation is thwarted by suboptimal catalyst selectivity and stability, and the lack of established structure–performance relationships. Systematic and controlled material nanostructuring offers an innovative approach for advancement in catalyst design. Herein low-valent manganese atoms stabilized on ceria, CeO_2 , are discovered as the first stable catalyst for NH_3 oxidation to N_2O , exhibiting two-fold higher productivity than the state-of-the-art. Detailed mechanistic, computational and kinetic studies reveal CeO_2 as the mediator of oxygen supply, while undercoordinated manganese species activate O_2 and facilitate N_2O evolution via N–N bond formation between nitroxyl, HNO , intermediates. Synthesis via simple impregnation of a small metal quantity (1 wt%) predominantly generates isolated manganese sites, while full atomic dispersion is achieved upon redispersion of sporadic oxide nanoparticles during reaction, as confirmed by advanced microscopic analysis and electron paramagnetic resonance spectroscopy. Subsequently, manganese speciation is maintained, and no deactivation is observed over 70 h on stream. CeO_2 -supported isolated transition metals emerge as a novel class of materials for N_2O production, encouraging future studies to evaluate their potential in selective catalytic oxidations at large.

1. Introduction

In view of the growing demand for green and sustainable technologies in the chemical industry, performing atom-efficient and selective oxidation reactions represents a key challenge.^[1–5] Nitrous oxide, N_2O , stands to play an important role in addressing this issue. While it is a well-established specialty chemical, primarily known for its use as an anesthetic, in the 1980s it has started to attract significant attention as a selective oxidizing agent. Owing to its ability to donate a single oxygen atom, it avoids the risk of over-oxidation and, notably, generates ecologically benign N_2 as the only by-product, positioning it as a green alternative to many conventional oxidizing agents.^[6–8] In the following years, N_2O has been shown to unlock unique pathways for the one-step oxidation of benzene to phenol or methane to methanol.^[9,10] The highly selective and facile nature of the former led to the implementation of the AlphOx process in the late 1990s. Therein, the Boreskov Institute

I. Surin, Z. Tang, S. Damir, S. Mitchell, J. Pérez-Ramírez
 Institute for Chemical and Bioengineering
 Department of Chemistry and Applied Biosciences
 ETH Zürich
 Vladimir-Prelog-Weg 1, Zürich 8093, Switzerland
 E-mail: jpr@chem.ethz.ch

J. Geiger, N. López
 Institute of Chemical Research of Catalonia (ICIQ)
 The Barcelona Institute of Science and Technology
 Av. Països Catalans 16, Tarragona 43007, Spain

H. Eliasson, R. Erni
 Electron Microscopy Center
 Empa – Swiss Federal Laboratories for Materials Science
 and Technology
 Überlandstrasse 129, Dübendorf 8600, Switzerland

M. Agrachev, G. Jeschke
 Laboratory of Physical Chemistry
 Department of Chemistry and Applied Biosciences
 ETH Zürich
 Vladimir-Prelog-Weg 1, Zürich 8093, Switzerland

F. Krumeich
 Laboratory of Inorganic Chemistry
 Department of Chemistry and Applied Biosciences
 ETH Zürich
 Vladimir-Prelog-Weg 1, Zürich 8093, Switzerland
 V. A. Kondratenko, E. V. Kondratenko
 Department of Catalyst Discovery and Reaction Engineering
 Leibniz-Institut für Katalyse
 Albert-Einstein-Straße 29a, 18059 Rostock, Germany

 The ORCID identification number(s) for the author(s) of this article can be found under <https://doi.org/10.1002/adma.202211260>.

© 2023 The Authors. Advanced Materials published by Wiley-VCH GmbH. This is an open access article under the terms of the Creative Commons Attribution-NonCommercial License, which permits use, distribution and reproduction in any medium, provided the original work is properly cited and is not used for commercial purposes.

DOI: 10.1002/adma.202211260

of Catalysis (BIC) and Solutia Inc. launched a pilot plant utilizing waste N_2O generated during manufacture of adipic acid, achieving 98% yield of phenol.^[6,7] Despite the success of the technology, no significant advances in the commercialization of N_2O -mediated processes have been made in the past two decades. The main reason for this is the lack of affordable N_2O . On the one hand, the existing N_2O streams (i.e., by-product of adipic acid production) contain only 30–40% N_2O and require extensive purification (removal of NO_x , CO_x , and O_2), entailing large capital and operational costs.^[11] On the other hand, almost all of the deliberately synthesized N_2O currently comes from thermal decomposition of ammonium nitrate, resulting in a prohibitively high price ($\approx 4000\$ \text{ t}^{-1}$).^[12] This is reflected in the limited scale of N_2O production, estimated to be $\approx 0.2\text{--}0.3 \text{ Mt year}^{-1}$ and expected to increase at the rate of only around 7% annually.^[13] The reason for this is the high cost of ammonium nitrate itself, which is a product of a complex and multi-stage manufacturing route, comprised of ammonia, NH_3 , oxidation to NO , its subsequent transformation into nitric acid, acid-base reaction with NH_3 and, finally, crystallization into a salt. Crucially, N_2O also forms as a minor by-product during the first stage of this process.^[14,15] Thus, by designing a suitable catalytic material and adapting the reaction conditions, the process of NH_3 oxidation can be tuned to yield N_2O as the main product, significantly reducing its price ($\approx 600\$ \text{ t}^{-1}$) and eliminating the need for downstream purification and allowing its application in existing or new selective oxidation reactions.^[12] Recent advances in the field of blue and green NH_3 production make this approach even more appealing, as they hold the potential to transform NH_3 oxidation to N_2O into a fully sustainable process, starting at the stage of feed-stock procurement and ending with the ultimate product application.^[16,17]

In an effort to design catalysts for NH_3 oxidation to N_2O , reducible metal oxides have been studied most extensively, owing to their inherent activity in redox reactions,^[18,19] with manganese-based systems being the most prominent.^[20,21] An important milestone was reached in 1998, with the identification of $\text{Mn-Bi-O}/\alpha\text{-Al}_2\text{O}_3$, the state-of-the-art catalyst at the time.^[22] This system, comprised of nm-sized particles of oxides of manganese, bismuth, and mixtures thereof and with a total metal content of 20 wt%, showed the highest N_2O selectivity ($\approx 83\%$) to date at nearly complete conversion of NH_3 .^[23,24] This result prompted the construction of a pilot plant by Solutia Inc. in collaboration with the BIC. However, despite the reported success of the test, the catalyst was never industrially implemented. The apparent reason for this was that Mn-Bi-O system performed optimally under an excess of O_2 , requiring its removal downstream and significantly increasing the costs. In contrast, the use of stoichiometric reactant amounts would likely have had a negative effect on the catalyst stability, as transition metal-based catalysts are known to suffer from deactivation due to over-reduction of the active phase^[15,24–27] — a key limitation of this class of materials.

In the following years, little advancement in the field of direct NH_3 oxidation to N_2O has been made. However, recently the topic experienced a revival, when our group reported small Au nanoparticles (2–3 nm) supported on ceria, CeO_2 , to be a highly selective and active material, far outperforming the

Mn-Bi-O system and setting a new benchmark for N_2O productivity.^[12] Remarkably, CeO_2 assumed the role of a co-catalyst, serving as the mediator of oxygen supply for the reaction, which proceeded via a Mars-van Krevelen-type mechanism at the interface between the support and Au. However, the catalyst suffered from deactivation due to agglomeration of Au nanoparticles. Furthermore, despite the superior activity of Au, the global trend toward making the chemical industry more sustainable demands a reduction in the use of precious metals. Thus, we adopted a new approach toward catalyst design, leveraging the newly gained understanding of the unique redox capabilities of CeO_2 , while utilizing well-established manganese as the active phase. Beyond simply using a cheaper and more abundant metal, this strategy aims to combine the specific redox properties of both phases, making it possible to engineer the active site at the atomic level, which can often give rise to new materials with unprecedented catalytic properties.^[28–30] Thereby, the long-standing problem of control over the nano-structure of NH_3 oxidation catalysts can be addressed.

Following this approach, we identify isolated, low-valent manganese atoms stabilized on CeO_2 as an outstanding catalyst for NH_3 oxidation to N_2O , outperforming Au nanoparticles in terms of selectivity, activity, and stability. The oxygen buffer ability of CeO_2 is found to be essential for the attainment of high N_2O productivity, providing abundant O species for the reaction. This is complemented by the ability of undercoordinated Mn^{2+} species on the surface of the support to effectively activate gas-phase O_2 and facilitate N–N bond formation, as evidenced by atomistic simulations. Furthermore, in contrast to the previously reported manganese-based systems, the high catalytic activity is attained with the total metal content of only 1 wt%. Atomic dispersion of the majority of manganese atoms is achieved during synthesis, proceeding via a simple impregnation method, while the few sporadic manganese oxide particles redisperse into single atoms over the course of the reaction. The resultant material remains subsequently unchanged, showing no loss of catalytic activity over 70 h on stream — an unprecedented result for an NH_3 oxidation catalyst to N_2O . Moreover, the remarkable oxidative properties of CeO_2 -supported atomically-dispersed transition metals presented here can extend beyond oxidation of NH_3 and find application in a range of other oxidation reactions. Thus, these findings are of significant relevance to the field of catalytic oxidations not only as an advancement in the production of an affordable and efficient oxidant, N_2O , but also as a demonstration of a novel type of material for selective oxidations at large.

2. Results and Discussion

2.1. Platform of Materials

To verify that manganese represents the most promising earth-abundant transition metal for NH_3 oxidation, a series of CeO_2 -supported transition metal catalysts were synthesized by incipient wetness impregnation (IWI) with a nominal metal content of 1 wt%. The reference catalysts were prepared following the synthetic procedures described in the respective studies.^[12,23] The catalytic performance of the derived materials

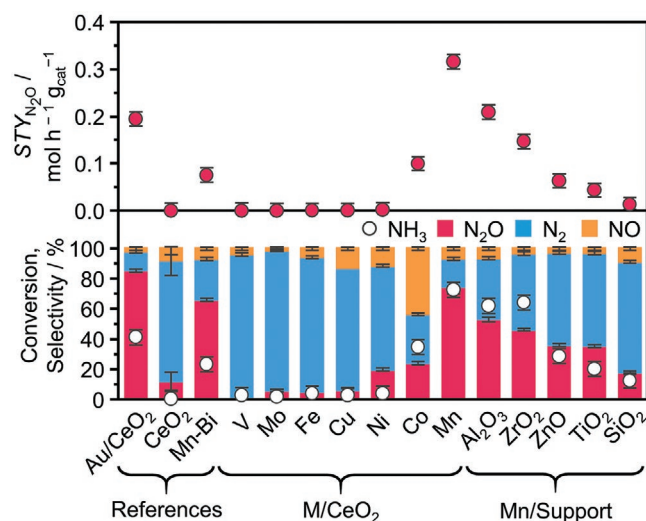


Figure 1. Catalytic performance in NH_3 oxidation of CeO_2 support and reference catalysts (References), transition metals supported on CeO_2 (Mn/CeO_2) and manganese supported on different carriers (Mn/Support), represented by the space-time yield (STY) of N_2O (top), NH_3 conversion and product selectivity patterns (bottom). Data presented as mean \pm 95% confidence interval ($n = 2$). Reaction conditions: $T_{\text{bed}} = 673 \text{ K}$; $m_{\text{cat}} = 0.04 \text{ g}$; $\text{GHSV} = 375000 \text{ cm}^3 \text{ h}^{-1} \text{ g}_{\text{cat}}^{-1}$; Feed = 8 vol.% NH_3 , 8 vol.% O_2 , 4 vol.% Ar, 80 vol.% He; $P = 1 \text{ bar}$. Au/CeO_2 and Mn-Bi were evaluated at 573 K and 623 K, respectively.

was subsequently evaluated in NH_3 oxidation. Reference systems showed performance metrics consistent with previous reports, thus providing a valid benchmark, while transition metal catalysts exhibited varying levels of NH_3 conversion and product selectivity (Figure 1). The majority showed very low activity and primarily formed N_2 , while Co/CeO_2 achieved appreciable NH_3 conversion, but also produced a much larger amount of NO ($S_{\text{NO}} > 20\%$). Accordingly, the poor catalytic performance of these systems disqualified them from further consideration in this work. However, in line with our expectations, manganese-based system achieved the highest N_2O selectivity, even rivaling that of the state-of-the-art Au/CeO_2 . In fact, Mn/CeO_2 exceeded the NH_3 conversion of the latter by a significant margin (73% vs 41%), thereby reaching a higher space-time yield of N_2O ($\text{STY}_{\text{N}_2\text{O}}$) than any previously reported material. Interestingly, the $\text{Mn-Bi/Al}_2\text{O}_3$ reference catalyst displayed an order of magnitude lower STY value, despite significantly larger manganese content (1 wt% vs 8.4 wt%). This suggests that manganese does appear to possess an inherent ability to catalyze the formation of N_2O from NH_3 , in accordance with previous literature reports. However, there remain other aspects of catalyst design, most prominently the choice of the support and the nanostructure of the active phase, which can have a profound effect on the catalytic footprint.

Accordingly, a platform of manganese catalysts on a selection of different carriers was synthesized by analogy with Mn/CeO_2 . Following the rationale of redox-active properties, supports ranging from non-reducible (i.e., Al_2O_3 , SiO_2) to partially-reducible (i.e., ZrO_2 , TiO_2) and reducible (ZnO) oxides were chosen. The resultant materials were then thoroughly characterized prior to testing. High-angle annular dark-field scanning

transmission electron microscopy (HAADF-STEM) coupled with energy dispersive X-ray spectroscopy (EDXS) revealed manganese to be highly dispersed on the surface of all supports except ZnO , where nanoparticles of MnO_x ($\approx 21 \text{ nm}$) were observed (Figure 4 and Figure S4, Supporting Information). Additionally, powder X-ray diffraction (XRD) analysis of the materials prior to and after manganese deposition showed identical reflection patterns (Figure S5, Supporting Information). This served as a further indication that the majority of manganese is likely present in the form of a largely amorphous MnO_x phase, and even the nanoparticles visible on ZnO are likely too small and too few in number (metal content = 1 wt%) to produce sufficiently sharp reflections. Temperature-programmed reduction with hydrogen (H_2 -TPR) analysis also complemented this notion, generally showing several ill-defined reduction peaks appearing over a wide range of temperatures, characteristic of a highly dispersed nature and heterogeneous speciation of manganese (Figure S6, Supporting Information).^[31] In the case of Mn/CeO_2 , the assignment of individual peaks to specific transformations of the active phase was further complicated by the redox-active nature of CeO_2 . Accordingly, surface reduction of CeO_2 strongly contributed to the superposition of peaks visible between 360 and 700 K.^[32] Furthermore, it appears that manganese deposition led to the onset of surface reduction at a lower temperature, which likely occurred due to a strong interaction between the metal and the lattice oxygen species, a well-documented phenomenon for CeO_2 -based catalysts.^[32–34] Conversely, Mn/ZnO showed a strong reduction peaks at 625 K, which can be attributed to transformations of $\text{Mn}_2\text{O}_3 \rightarrow \text{MnO}$.^[35] Such behavior is consistent with the presence of nanoparticles seen by EDXS mapping. Finally, X-ray photoelectron spectroscopy (XPS) analysis of $\text{Mn } 2p_{3/2}$ revealed a diverse electronic structure of manganese in all samples, with metal oxidation state ranging from Mn^{2+} to Mn^{4+} present in varying amounts (Figure S8, Supporting Information). Remarkably, in Mn/CeO_2 low-valent manganese (i.e., Mn^{2+}) was most abundant, which is in line with previous reports on the ability of CeO_2 to strip oxygen from manganese at temperatures above 700 K.^[36] This process likely occurred during sample calcination ($T = 823 \text{ K}$), resulting in manganese being primarily stabilized in the reduced form. This point is further corroborated by the position of the peak being shifted towards lower binding energy values (640.9 eV) relative to other catalysts and the presence of a prominent satellite feature at $\approx 647 \text{ eV}$, characteristic of Mn^{2+} .^[37]

With structural differences and commonalities between the catalysts established, their performance in NH_3 oxidation was assessed and differences in activity and N_2O selectivity could be observed, with the CeO_2 -supported system outpacing its counterparts (Figure 1). Still, the catalysts do share some common features, such as the fact that N_2O selectivity is generally maximized at 673 K (Figure S2, Supporting Information) and increases alongside NH_3 conversion (Figure S3, Supporting Information). This is an important practical consideration, as it enables operation under optimal conditions without the need to recycle unreacted NH_3 . This trend also suggests that there is likely to be a specific material property, which could serve as a descriptor of both activity and selectivity, and thus guide the rational design of a superior material.

2.2. Structure–Performance Relations

In order to understand the origin of the diverging behavior of manganese-based catalysts and identify relevant structure–performance relationships, we first considered the ability of the catalysts to interact with gas-phase O_2 as a necessary factor for attaining high catalytic activity. Namely, by performing volumetric O_2 chemisorption at 673 K, the quantity of adsorbed oxygen, herein referred to as the oxygen uptake, could be quantified. Notably, this property clearly depends on both the redox properties of the support, as evidenced by negligible oxygen uptake values of all pristine carriers except CeO_2 , and the manganese speciation, as is evident from the correlation with the valence of manganese, determined by XPS (Figure 2a,b). This observation was rationalized by considering manganese valence as a degree of oxygen saturation, and thus low-valent surface manganese species can accommodate more oxygen ligands. In this regard, it must be noted a significant increase in the oxygen uptake of CeO_2 would also be expected upon doping with a heteroatom,^[12] which could happen if manganese substituted cerium atoms during calcination. However, penetration of manganese into even the surface layer of CeO_2 would entail manganese assuming a higher oxidation state (vide infra), which was not reflected by the XPS analysis, therefore suggesting that undercoordinated manganese is indeed present on the catalyst surface. Additionally, the quantities of O_2 adsorbed either physically or chemically can be easily differentiated

using this technique, where the latter represents the amount of oxygen that forms a bond with the catalyst surface. This value was used for quantification of the oxygen uptake. It must also be emphasized that the measurements were carried out at 673 K, that is, the temperature of the reaction. Hence, the determined values of oxygen uptake are representative of a material's ability to activate O_2 under the reaction conditions, and thus can be related to the observed catalytic performance. In this respect, a correlation between the oxygen uptake of different catalysts and their corresponding selectivity to N_2O and STY_{N_2O} could be identified (Figure 2c,d). Accordingly, the principal role of oxygen uptake here can be interpreted on the basis of the reaction mechanism, which must comprise oxidative dehydrogenation of NH_3 , followed by oxidation of NH_x fragments to ultimately yield N_2O . As all manganese catalysts exhibited modest NO selectivity (< 5%) due to the relatively low reaction temperature, the main discrepancy between them consisted in the relative quantities of N_2 and N_2O produced. As the latter contains a more oxidized form of nitrogen, it stands to reason that oxygen availability is of central importance to the ability of a material to promote N_2O formation.

To further validate this hypothesis, kinetic analysis of the catalyst platform was performed. Namely, by systematically varying the reaction temperature or the partial pressure of a given reactant, the apparent activation energy and the reaction orders with respect to each reactant were derived (Figure S7, Supporting Information). The latter reflects how the respective

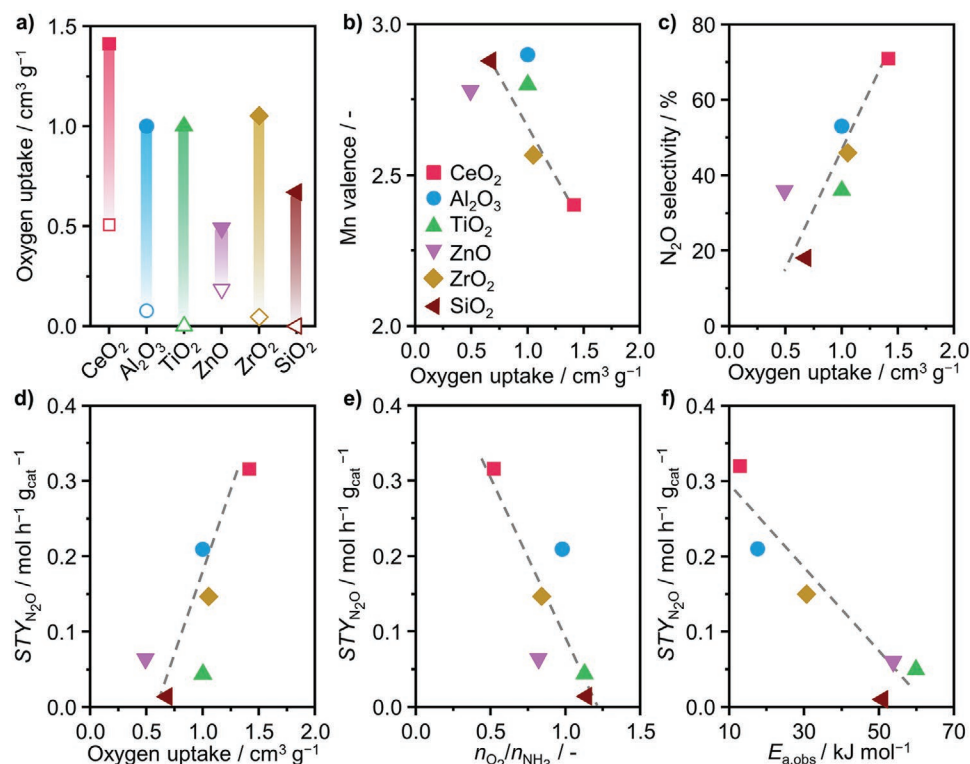


Figure 2. Performance descriptors of Mn/Support catalysts. a) Oxygen uptake of bare supports (open symbols) and after depositing manganese (solid symbols), determined by volumetric O_2 chemisorption; b) Mn valence, determined by XPS, and c) N_2O selectivity as a function of oxygen uptake; STY_{N_2O} as a function of d) oxygen uptake, e) the ratio of O_2 and NH_3 reaction orders; and f) the apparent activation energy. Reaction conditions: $T_{bed} = 673$ K; $m_{cat} = 0.04$ g; $GHSV = 375\,000$ $cm^3 h^{-1} g_{cat}^{-1}$; Feed = 8 vol% NH_3 , 8 vol% O_2 , 4 vol% Ar, 80 vol% He; $P = 1$ bar.

concentrations of the reactants affect the observed rate of reaction. Given that both reactants must be adsorbed on the catalyst surface for the reaction to occur, the difference in the reaction orders can give an indication of the relative abundance of each species on the catalyst surface under typical reaction conditions. For instance, if $n(\text{O}_2)$ is larger than $n(\text{NH}_3)$, we can interpret this in terms of the availability of NH_3 for the reaction exceeding that of O_2 , and hence the rate of reaction is more strongly affected by a change in O_2 partial pressure. Furthermore, as the stoichiometry of NH_3 oxidation toward N_2 , N_2O , and NO varies, with each product requiring progressively larger quantity of O_2 , we can expect that the selectivity profile of a catalyst will depend on the relative ratio of the two reaction orders as well. Following this rationale, the ratio of $n(\text{O}_2)/n(\text{NH}_3)$ was calculated and plotted against $STY_{\text{N}_2\text{O}}$ (Figure 2e) for each manganese catalyst. In agreement with our expectation, a good correlation was obtained, suggesting that the ability of a catalyst to activate O_2 plays a decisive role in determining its activity and selectivity to N_2O . This is also in accordance with the previously established relation between $STY_{\text{N}_2\text{O}}$ and oxygen uptake, further validating it as a performance descriptor. Finally, the apparent activation energy of the reaction could also be correlated with $STY_{\text{N}_2\text{O}}$, leading to the conclusion that oxygen activation is likely to be the rate-limiting step of the reaction as well (Figure 2f).

2.3. Mn/CeO₂ Catalyst for N₂O Synthesis

Having established the underlying reason for the observed differences in catalytic activity and selectivity, catalyst stability in NH_3 oxidation was also evaluated for 70 h on stream. The resultant profiles showed significant variations in terms of both the rate of the initial activity loss and the overall drop in $STY_{\text{N}_2\text{O}}$ during the test (Figure 3a). Accordingly, Mn/SiO₂ and Mn/ZnO rapidly deactivated during the first 10 h of the reaction, losing over 50% of their initial activity. At the same time, most of the remaining catalysts experienced a gradual drop in $STY_{\text{N}_2\text{O}}$. Mn/CeO₂ stands in contrast to all other materials, as it actually underwent an induction period during the initial ≈ 20 h of the reaction, during which a minor increase in selectivity and activity was observed (Figure S9, Supporting Information). Subsequently, a stable mode of operation was achieved and maintained throughout the entire duration of the test. This is a remarkable result, as both reference catalysts showed significant deactivation under identical reaction conditions, thus setting Mn/CeO₂ apart as not only a highly productive, but also a robust catalyst. It must also be noted that the conditions of the stability test, namely the gas-hourly space velocity (GHSV), were much harsher than the typical values reported in the literature.^[38,39] Therefore, the apparently relatively short duration of the test (70 h) nevertheless allows for a valid assessment of catalytic stability.

To gain insights into the structural changes that underpin the observed stability trends, HAADF-STEM, EDXS, and XPS analyses of the material after 70 h on stream were carried out. The acquired microscopy images and elemental maps clearly evidenced manganese agglomeration in all samples except Mn/CeO₂ and Mn/ZrO₂ (Figure 4 and Figure S10, Supporting

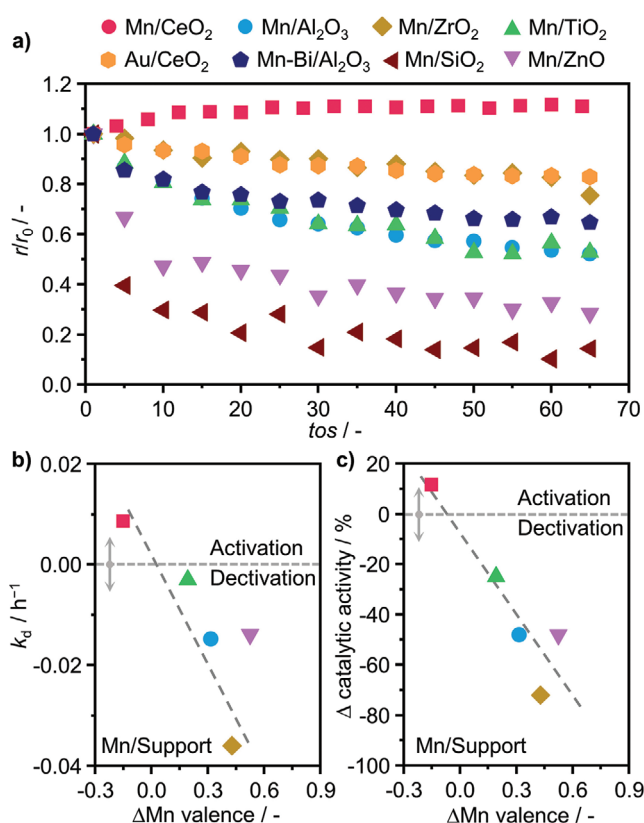


Figure 3. a) Stability test of selected catalysts. While all other systems exhibit varying rates of deactivation, Mn/CeO₂ undergoes an induction period, gaining activity and subsequently stabilizing; b) deactivation constant k_d and c) loss of catalytic activity of supported Mn catalysts as a function of change of Mn valence after 70 h on stream. Reaction conditions: $T_{\text{bed}} = 673 \text{ K}$; $m_{\text{cat}} = 0.04 \text{ g}$; $\text{GHSV} = 375\,000 \text{ cm}^3 \text{ h}^{-1} \text{ g}_{\text{cat}}^{-1}$; Feed: 8 vol% NH_3 , 8 vol% O_2 , 4 vol% Ar, 80 vol% He; $P = 1 \text{ bar}$.

Information). The latter two appeared to maintain the high degree of manganese dispersion, despite Mn/ZrO₂ still deactivating, albeit to a lesser extent than others. Mn $2p_{3/2}$ XPS analysis of the used catalysts led to a rather unexpected result, revealing that manganese in nearly all samples was oxidized (Figure S8, Supporting Information). In fact, the only catalyst which experienced a decrease in manganese valence is Mn/CeO₂, which consistently enhanced the activity. This is in direct opposition to the commonly accepted notion that transition metal-based catalysts primarily suffer from deactivation due to reduction under the reaction conditions. Still, in view of the observed changes of manganese nuclearity, it is possible that the overall increase in manganese valence was inextricably linked to the agglomeration process. Nevertheless, the importance of maintaining manganese in the low-valent state is evident—a clear correlation between both the rate of the initial deactivation and the overall decrease in catalytic activity with the change in the average oxidation state was found (Figure 3b,c). We can therefore conclude that preserving the highly dispersed nature of manganese is advantageous from the standpoint of both atomic efficiency, and as a way of maintaining the optimal metal speciation. Consequently, Mn/CeO₂ warranted a more detailed investigation, as its stability not only positions it as a

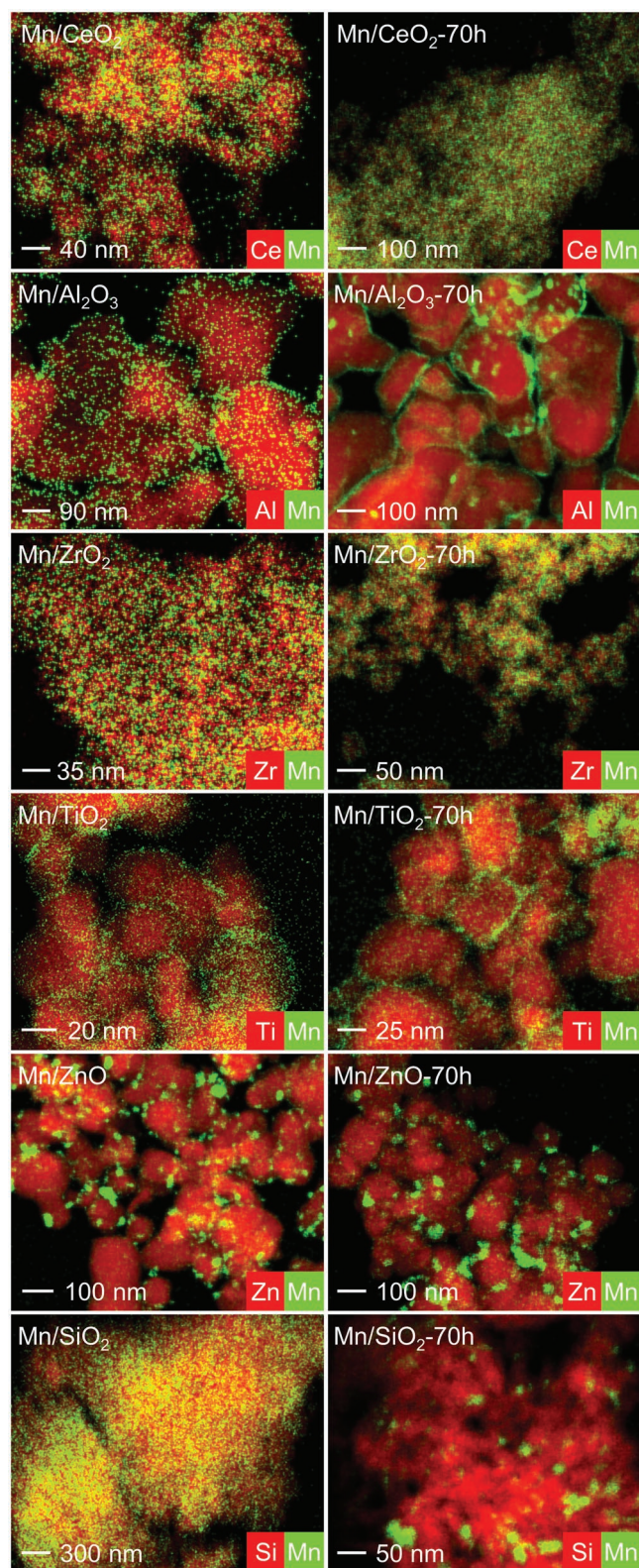


Figure 4. STEM-EDX maps of as-prepared and used Mn/Support catalysts.

practically relevant system for potential commercialization, but also as one of fundamental interest, offering a platform to study the nature of the active site.

2.4. Manganese Speciation in Mn/CeO₂

While the highly distributed nature of manganese was apparent based on the elemental mappings shown in Figure 4, the exact nanostructure of the metal could not be fully discerned. Accordingly, a more detailed microscopic analysis of both the fresh and the used sample was conducted, comprising high-resolution STEM (HRSTEM) and EDXS mapping (Figure 5a,b). An extensive HRSTEM search was carried out looking at the surface and edges of well-defined CeO₂ flakes, but no manganese particles were found. Single manganese atoms and clusters of a few atoms are not visible in the HAADF images due to the much higher atomic mass of cerium. Still, the presence of manganese was confirmed by the integrated EDXS spectra (Figure S11, Supporting Information). By analyzing the corresponding elemental maps, the manganese signals appeared to be evenly scattered across the entire surface of CeO₂, which, given the scale of the images, suggested that manganese could be present in the form of isolated atoms.

To further substantiate the claim of atomic dispersion of manganese in Mn/CeO₂, electron paramagnetic resonance (EPR) spectroscopy was employed as a means of probing the degree to which EPR-active species (i.e., Mn²⁺ and Mn⁴⁺) are magnetically, and hence spatially, isolated. Accordingly, the EPR spectrum of as-prepared Mn/CeO₂ was measured at room temperature and showed a very broad (with a linewidth of almost 3000 G) signal centered at around 1800 G (Figure 5d). Contrary to the expectations, such broad, anisotropic, and low-field-centered signals are typical for magnetically ordered systems with strongly exchange-coupled paramagnetic ions. This is confirmed by the change of the spectrum observed after changing the sweep direction (i.e., up: from low to high field, down: from high to low field). This magnetic hysteresis clearly indicates that the signal can be attributed to the presence of ferro/antiferromagnetic particles. In order to identify the latter, a series of additional measurements were performed at different temperatures (Figure S13, Supporting Information). A clear decrease of the signal intensity was observed with lower temperatures, which is characteristic of antiferromagnetic systems. By plotting the reciprocal of the peak-to-peak amplitude, which roughly estimates the magnetic susceptibility, a Néel temperature (i.e., temperature at which antiferromagnetic ordering takes place) of ≥ 130 K was determined. This leads to the conclusion that this signal stems from nm-sized MnO nanoparticles, in which Mn²⁺ ions are antiferromagnetically coupled.^[40,41] Nevertheless, an additional signal was observed at around 3500 G (g factor $g = 2.006$), consisting of six lines of almost equal intensity, split by about 92 G. This signal is typical for magnetically-diluted Mn²⁺, with the splitting due to the hyperfine interaction between electron and nuclear spin ($S = 5/2$, $I = 5/2$, respectively). The signal can therefore be attributed to atomically-dispersed Mn²⁺ on the surface of CeO₂. The narrow lines indicate that the dipole–dipole interactions between Mn²⁺ are relatively weak, which indicates that a significant fraction of manganese is still highly dispersed, despite the presence of some amount of MnO.

The spectrum of the used sample acquired at room temperature also showed the two manganese-related components. However, in contrast to the as-prepared material, the MnO

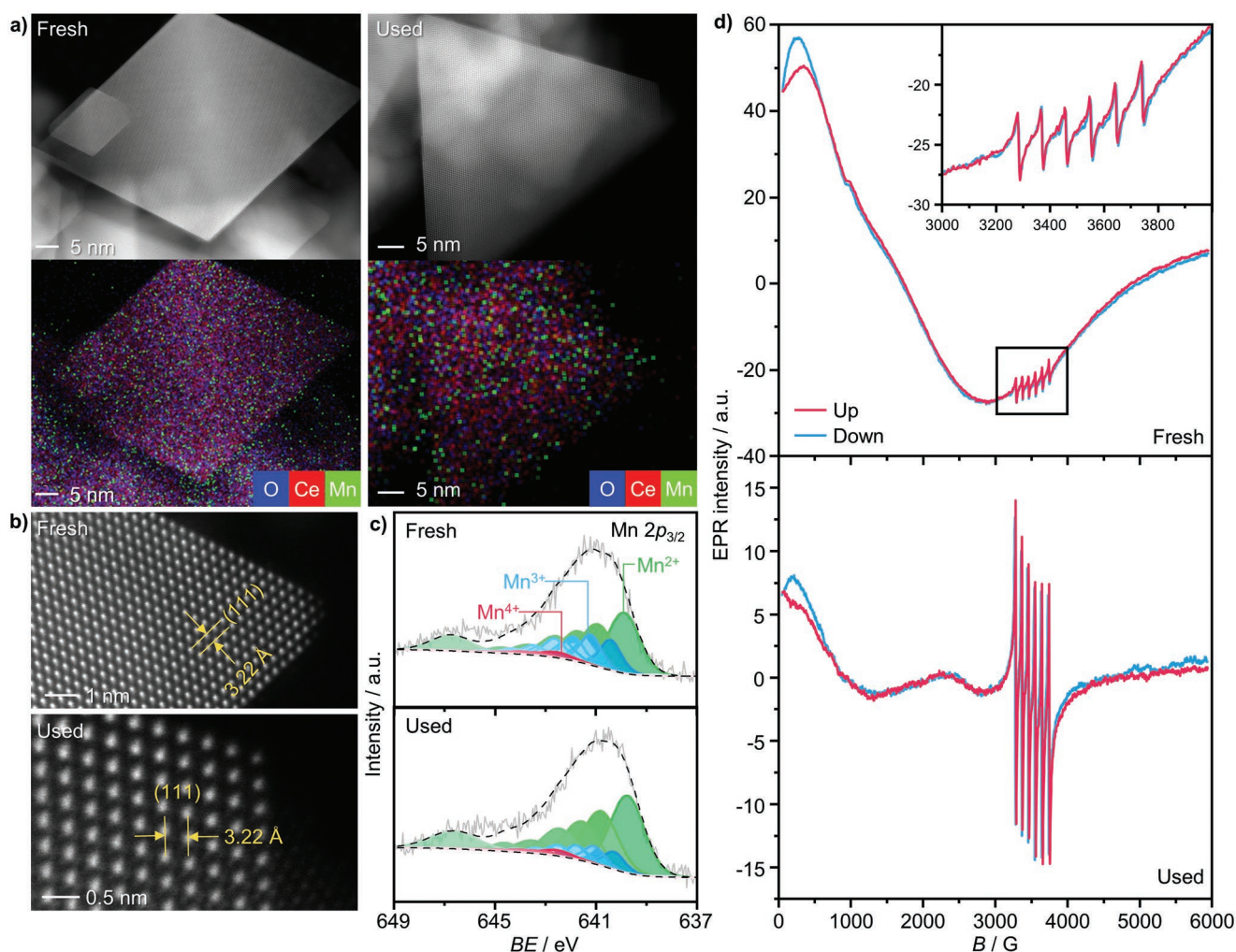


Figure 5. Characterization of as-prepared Mn/CeO₂ and after 70 h on stream. a) HAADF-STEM micrographs with EDX maps, b) HRSTEM images, and c) Mn 2p_{3/2} XPS spectra demonstrate that the highly dispersed low-valent nature of manganese is maintained during the reaction. d) Both EPR spectra evidence hyperfine splitting, characteristic of large quantities of isolated Mn²⁺ species. Disappearance of the broad signal, characteristic of bulk MnO, after the reaction suggests that redispersion occurred and full atomic dispersion was achieved.

signal practically disappeared, while the signal of isolated Mn²⁺ species became much stronger. Such changes in the intensity of the signals may arise either from redox processes between paramagnetic (i.e., EPR-active) and diamagnetic (i.e., EPR-silent) states or from nuclearity changes, which can lead to interconversion between paramagnetic (isolated sites) and antiferromagnetic (particles) signals. From Mn 2p_{3/2} XPS analysis it is evident that manganese undergoes reduction during the reaction (Figure 5c). Therefore, if we only consider the redox processes, they would lead to an increase of the MnO signal. However, the opposite was observed, which instead suggests that redispersion of MnO into isolated Mn²⁺ species took place. This is also the likely origin of the observed induction period during the stability test. Additionally, the increase of the Mn²⁺ signal could be attributed not only to redispersion of MnO, but also to the transformation of isolated Mn³⁺ species into Mn²⁺.

To further validate these conclusions, EPR spectra of Mn/Al₂O₃ at room temperature were also acquired (Figure S14,

Supporting Information). The as-prepared sample showed a very similar, but significantly stronger MnO signal. No Mn²⁺ signal was observed in this case. This indicates a lower dispersion degree, compared to Mn/CeO₂. After the reaction, the MnO signal decreased, but its intensity was still quite strong. However, as evidenced by Mn 2p_{3/2} analysis, in contrast to Mn/CeO₂, Mn/Al₂O₃ gets significantly more oxidized with time on stream. Therefore, in this case, the decrease in the intensity of the MnO signal could be attributed to the transformation of Mn²⁺ into Mn³⁺. Indeed, this is more consistent with the microscopy analysis, which shows significant agglomeration of manganese (Figure 4 and Figure S10, Supporting Information). In addition, a narrow, unstructured line appears at $g = 2.006$ after the reaction, which can be attributed to Mn²⁺ species still present on the surface of Al₂O₃. Unlike in Mn/CeO₂, however, the hyperfine splitting here is completely unresolved because the lines are significantly broader. This is due to stronger Mn²⁺–Mn²⁺ dipolar interactions and indicates that the degree of spatial isolation is lower than in Mn/CeO₂.

On the basis of the acquired spectroscopic and microscopic insights, we affirm that Mn/CeO₂ constitutes a single-atom catalyst (SAC), being the first material of this class for NH₃ oxidation to N₂O. After synthesis, the as-prepared sample still has a small degree of nanostructure heterogeneity, exhibiting sporadic MnO nanoparticles, albeit so few in number that they could not be detected in any of the micrographs. However, upon exposure to the reaction conditions, full atomic dispersion was achieved, ultimately giving rise to a distribution of Mn²⁺ and Mn³⁺ stabilized on the surface of the catalyst. Furthermore, in view of the catalytic inertness of CeO₂ alone, and the observed induction period during the stability test, attributed to in situ redispersion, we propose that isolated manganese atoms act as the active sites of the reaction. Therefore, having established the likely structure of the latter, we were presented with a unique opportunity to also study the mechanism of the reaction, which could potentially reveal new guidelines for catalyst design and optimization.

2.5. Mechanistic Insights

It is generally accepted that the mechanism of low-temperature NH₃ oxidation must involve two key steps, namely the oxidative dehydrogenation of NH₃ (Equations (1) and (2)) and subsequent oxidation of the NH_x fragments to a nitroxyl intermediate, HNO (Equation (3)).^[24,42–45] The latter has long been postulated to be central in the formation of N₂O, which proceeds via the recombination of two HNO species (Equation (4)).



Conversely, if oxygen supply is insufficient, NH_x fragments may proceed to react with each other or HNO, thereby forming N₂ as the main product (Equations (5)–(7)).



While only limited experimental or computational evidence exists to support this scheme, it is nevertheless in good agreement with the observation that the catalyst's ability to provide active oxygen species results in the superior capacity to selectively generate N₂O.^[12] Thus, we adopted this reaction sequence as a starting point for the investigation of the mechanism over isolated manganese sites, using density functional theory (DFT).

For this purpose, we first evaluated all possible adsorption sites for manganese atoms on the low-index (100), (110), and (111) facets of CeO₂, considering on-top, bridge, and hollow adsorption sites (Figure S15, Supporting Information), as well as substitutional lattice positions. Structural optimizations for these 20 possible catalyst structures were done with the Perdew–Burke–Ernzerhof (PBE) functional, using a Hubbard U-correction

for the cerium cations.^[46] Overall, we find that on all facets, feasible coordination motifs for the stabilization of single-atom Mn exist (Figure S16, Table S5, Supporting Information). We then assigned formal manganese oxidation states (OS) by counting reduced Ce³⁺ centers (polarons) in the support, revealing the strong correlation between the number of oxygen ligands and the manganese oxidation state (Figure S16, Supporting Information). Formal OS assignments were further verified by Bader charges and simulated XPS shifts (Figure S17, Supporting Information).^[47–49] However, we found that Mn/CeO₂ presents a highly complex electronic structure, due to the charge transfer between manganese and CeO₂ that leads to a variable oxidation state of the former and a variable number (and distribution) of reduced Ce³⁺ centers in the support. Therefore, while for many applications the PBE+U method offers balanced cost-efficiency performance, a more sophisticated method including exact exchange (i.e., hybrid method) is required to assess the energies for the Mn/CeO₂ interface. This comes at a price of at least one order of magnitude higher computational cost and the impossibility to re-optimize the structures, thus limiting our investigation to a thermodynamic assessment of the reaction mechanism. Thus, we further refined adsorption energy estimates with the HSE03-13 hybrid functional based on the PBE+U optimized structures.^[50–53] Importantly, we find that highly oxidized manganese states are overstabilized when using PBE+U (Table S5, Supporting Information). For instance, on CeO₂(111), the exothermicity of single-atom adsorption increases with the formal Mn-OS. This is in contrast to HSE03-13, which yields Mn²⁺ as the only stable structure on this facet. It should further be noted that the discrepancies for the substitutional catalyst models are less severe as they do not contain reduced Ce³⁺ centers. Thus, we deem energy differences for structures with a fixed numbers of Ce³⁺ centers to be reliable, even at the PBE+U level.

From the retained potential catalyst structures (Figure S16, Supporting Information), we then turned our attention to the investigating of possible reaction pathways towards the formation of N₂O. Although manganese is likely a mixture of various species, XPS points to manganese being mainly present in a low-valent state, particularly after stabilization on stream (Figure 5c). Thus, we selected Mn²⁺ on all three low-index facets, as well as the two lowest-energy Mn³⁺ structures on (110) and (100) (models a–e in Figure S16, Supporting Information and Figure 6a) as representative reaction sites. This reduced set of five possible Mn-SAC structures encompasses all low-index ceria surfaces, as well as coordination patterns ranging from two to four oxygen atoms, and was then used to investigate adsorption of the reactants, O₂ and NH₃, as well as the proposed HNO intermediate. Additionally, the stability of a hyponitrous acid, H₂N₂O₂, cyclic intermediate was investigated. It is the protonated form of a hyponitrite, N₂O₂²⁻ ion, commonly accepted to form during NO coupling in nitric oxide reductase (NOR) enzymes, followed by decomposition into N₂O.^[54–56] Given the single-atom nature of the catalyst, the manganese site could potentially act in an analogous fashion to the enzymatic metal center of an enzyme and promote the combination of HNO species to yield N₂O.

Adsorption energies were evaluated both with PBE+U and refined at the higher level HSE03-13 hybrid functional and

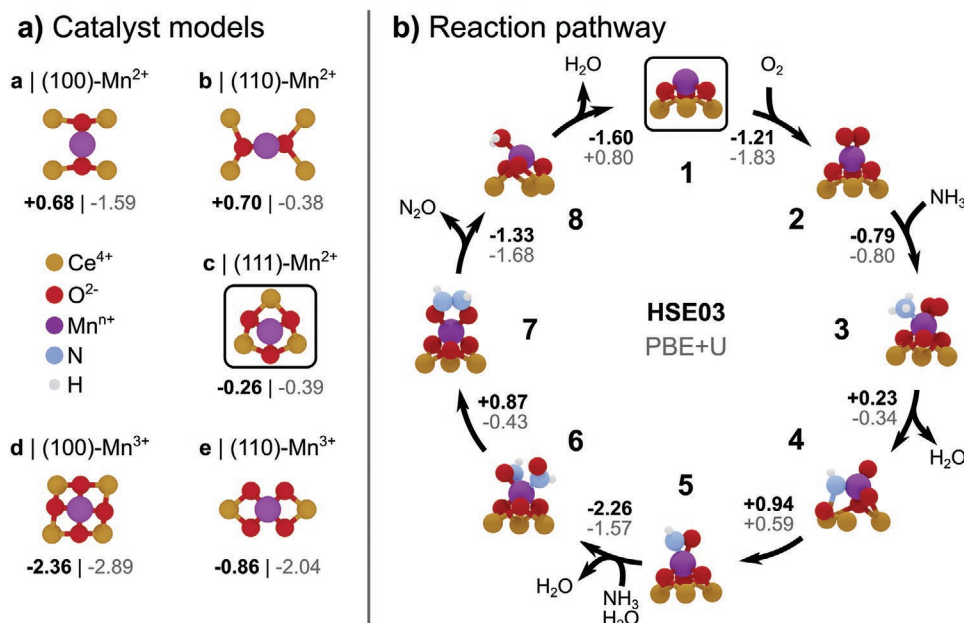


Figure 6. Computational exploration of the reactivity landscape. a) Representative Mn-SAC structures on low-index ceria facets, encompassing varied coordination motifs and manganese oxidation states. b) Proposed reaction pathway proceeding via nitroxyl, HNO, and *cis*-hyponitrous acid, $\text{H}_2\text{N}_2\text{O}_2$ intermediates for the most stable Mn^{2+} catalyst structure on the most abundant exposed (111) facet. Single-atom adsorption energies and reaction energies between intermediates along the reaction sequence are indicated. All energies are given in eV.

are summarized in Table S7, Supporting Information. First, we note that both molecular and dissociative O_2 adsorption on low-valent Mn is highly exothermic for all three ceria facets (Figure S18a, Supporting Information), proving its inherent ability activate gas-phase O_2 , and to provide reactive oxygen species necessary for the reaction. Second, we find that low-coordinated Mn^{2+} (models a–c in Figure 6a) allows for the stabilization of a *cis*-hyponitrous acid intermediate via the formation of a κ^2 -coordinated ring structure. This is a crucial step for N–N bond formation en route to the main observed products, N_2O , and N_2 .^[57–59] On the four-fold coordinated Mn^{3+} (models d–e in Figure 6a), on the other hand, this process is hindered by the saturated coordination of the manganese to the support.

Finally, from the wealth of the obtained data, we could construct a thermodynamically plausible reaction pathway for the full selective catalytic cycle, schematically shown for Mn^{2+} on (111), (structure 1 in Figure 6b). It should be noted that the arrows along the cyclic reaction path do not denote elementary steps, but rather serve to connect key intermediates used to evaluate thermodynamic viability. Importantly, the reaction sequence proceeds via previously proposed HNO and $\text{H}_2\text{N}_2\text{O}_2$ intermediates, and indeed follows a similar route as the formation of N_2O by nitric oxide reductase (NOR) enzymes. First, exothermic adsorption (–1.21 eV) and activation of gas-phase O_2 leads to intermediate 2 (Figure 6b). The low-valent nature of manganese allows for co-adsorption of NH_3 , which completes its octahedral coordination sphere. Subsequently, NH_3 dehydrogenation is facilitated by the activated nature of O_2 (Figure S18a, Supporting Information) and driven by H_2O elimination. In the resulting intermediate 3, the NH fragment is stabilized by coordination to an adjacent cerium center of the support, while one reactive oxygen atom remains bound to manganese. The

formation a first η^2 -coordinated HNO fragment, intermediate 5, requires the endothermic (+0.94 eV) formation of the N–O bond.

We then assume the formation of another HNO proceeding in a similar fashion, consuming another NH_3 and O_2 pair, while eliminating H_2O , and finally resulting in intermediate 6. In this structure, asymmetric coordination of the two HNO moieties again leads to octahedral coordination around the manganese atom. Crucially, the simultaneous coordination of two HNO fragments to low-valent manganese brings them in proximity to facilitate N–N bond formation (+0.87 eV), which results in the *cis*-hyponitrous acid intermediate 7. Interestingly, in this structure, one of the Mn–O bonds to the ceria support is significantly elongated (2.41 Å) such that the coordination around the manganese atom can best be described as square planar. Evidently, the dynamic coordination to the $\text{CeO}_2(111)$ support allows the manganese atom to adapt its geometry during the reaction sequence. Lastly, from the *cis*-hyponitrous acid fragment, intermediate 7, N_2O can be released (intermediate 8), with elimination of H_2O recovering the catalyst in its initial state.

It should be noted that along the proposed reaction sequence (Figure 6b) different acid-base equilibria for the intermediates 5 to 7, involving ligand and/or lattice oxygen, are likely to influence the rate. Similarly, under operating conditions, the direct participation of reactive lattice oxygen originating from CeO_2 in a surface Mars-van Krevelen type mechanism is likely (Figure S19, Supporting Information). While we have evaluated some alternative structures, presented in Figures S18b,c, Supporting Information, these processes open up an intractable number of additional reaction pathways, far exceeding the scope of the present work, and warranting separate, dedicated investigations.

Lastly, we could also obtain analogous, thermodynamically, feasible reaction pathways (Figure S20, Supporting Information) for Mn^{2+} catalysts on the (100) and (110) facets (models a and b in Figure 6a), hinting at the inherent capability of low-valent single-atom Mn to facilitate N_2O formation.

To experimentally investigate the role of lattice oxygen of CeO_2 in the course of NH_3 oxidation to N_2O , a suitable method to monitor the onset of the reaction under relevant conditions was required. As oxidation of NH_3 proceeds very quickly and evolves a large amount of heat, temporal analysis of products (TAP) was chosen as a suitable tool to study the interactions of the reactants and the product formation under isothermal conditions.^[60,61] A further advantage of TAP is the ability to pulse small quantities of the reactants (in the order of 10^{-9} mol), thereby making it possible to monitor the initial catalytic behavior of a material and potentially observe the most prominent involvement of oxygen species from CeO_2 . To this end, an equimolar mixture of He, NH_3 , and $^{18}\text{O}_2$ was pulsed over Mn/CeO_2 in the temperature window of 473–773 K. Despite the quantitative difference in product distribution between steady-state and TAP experiments, likely arising as a result of the large pressure gap, the general selectivity trends were consistent, with the highest quantity of N_2O formed at 673 K, while the amount of NO produced steadily increased with reaction temperature (Figure 7a). Remarkably, the quantity of ^{16}O -containing products, that is, N^{16}O and N_2^{16}O , significantly exceeded that of N_2^{18}O and N^{18}O , indicating that direct participation of oxygen originating from CeO_2 took place. Furthermore, the identical shape of the signals for products containing labelled and non-labelled oxygen indicate that their formation proceeds at the same rate. This implies that $^{18}\text{O}_2$ likely healed the oxygen vacancy formed when lattice oxygen of CeO_2 participated in NH_3 oxidation, and was incorporated into another

N_2O molecule as a lattice specie upon subsequent reaction. We also observed two distinct signals at mass to charge ratio (m/z) of 18 and 20, which could be attributed to H_2^{16}O and H_2^{18}O molecules, respectively (Figure 7b). Despite $^{18}\text{O}_2$ contributing to the signal at m/z 18 as doubly ionized ion, the different shapes of the responses related to m/z 36 and 18 prove that H_2^{16}O is formed. Thus, lattice oxygen species of CeO_2 also participated in oxidative dehydrogenation of NH_3 . However, it should be noted that the origin of labelled and non-labelled oxygen in the H_2O molecules is different. As the peak of H_2^{18}O appears after that of H_2^{16}O , the formation of the former proceeds slower. This suggests that $^{18}\text{O}_2$ participates in the initial dehydrogenation of NH_3 as adsorbed and not lattice species, albeit to a lesser degree, as can be inferred from the relatively noisier signal of H_2^{18}O .

Given the presence of sporadic MnO particles in the fresh sample of Mn/CeO_2 , it also had to be verified that it is indeed the lattice of CeO_2 that acts as the source of ^{16}O atoms. Accordingly, we have conducted analogous TAP pulse experiments on $\text{Mn/Al}_2\text{O}_3$. Interestingly, in this case we have also observed an appreciable amount of ^{16}O -containing products, however, it is still significantly lower than that found in Mn/CeO_2 , particularly at higher temperature (Figure 7c). In view of the non-reducible nature of Al_2O_3 , the non-labelled oxygen atoms must have originated from the supported manganese oxide phase. Notably, participation of lattice O in NH_3 oxidation has also been reported for a TiO_2 -supported manganese catalyst.^[62] Therefore, we cannot exclude that MnO particles found in Mn/CeO_2 also contribute to the product formation via a Mars-van Krevelen mechanism. However, given the significantly higher intensity of manganese oxide signal in the EPR spectrum of $\text{Mn/Al}_2\text{O}_3$ as compared to Mn/CeO_2 (Figure 5, S 14), and the smaller amount of ^{16}O -containing products formed over the former, we can deduce that CeO_2 is still the primary origin of oxygen species for NH_3 oxidation over Mn/CeO_2 . On the basis of these findings, we can conclude that the process of N_2O formation over Mn/CeO_2 proceeds via a surface Mars-van Krevelen-type mechanism. This observation is in line with our previous findings on Au/CeO_2 , serving as another example of atomically dispersed metal species activating surface lattice oxygen of the support for catalytic oxidations,^[63,64] and highlighting the role of CeO_2 as an integral component of the catalyst.

Notably, the observation that oxygen species of manganese oxide can be involved in the product formation potentially offers interesting insights into the previously mentioned redispersion of manganese oxide particles in Mn/CeO_2 . Strategies for the redispersion of metallic nanoparticles through alternating reducing and oxidizing treatments are well-established in the literature.^[65,66] These typically describe a “strain” model, where oxidation of the outer layer of a metallic nanoparticle induces metal strain energy, prompting the fragmentation of the large particle into smaller species, which then undergo dispersion through interactions with the carrier. Although in the case of Mn/CeO_2 the particles are not metallic, it is possible that the inversion of the mechanism described above could be the reason for the observed redispersion. Namely, through the removal of oxygen atoms from the outer layer of the manganese nanoparticle via NH_3 oxidation, the outer layer is reduced, resulting in generation of strain. This, coupled to the high exo-

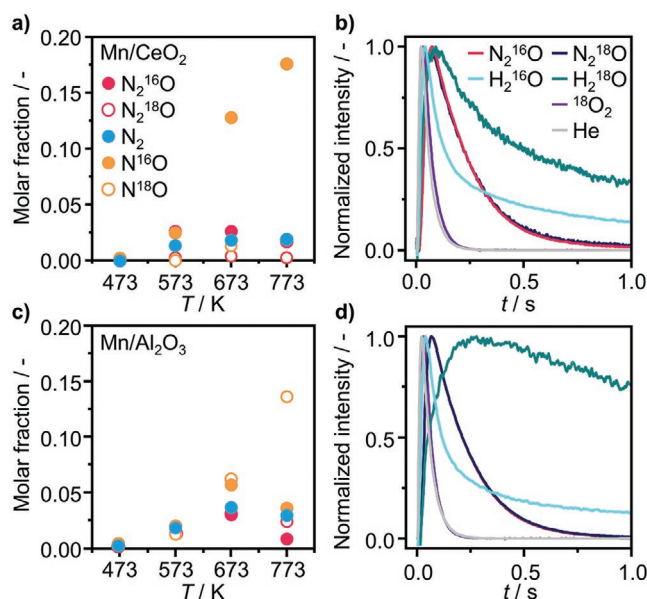


Figure 7. Temporal analysis of products (TAP) of NH_3 oxidation over Mn/CeO_2 and $\text{Mn/Al}_2\text{O}_3$. a,c) Product distribution as a function of temperature and b,d) transient response at 673 K after pulsing of 1:1:1 NH_3 : $^{18}\text{O}_2$:He mixture.

thermicity of NH_3 oxidation, and previously established ability of CeO_2 to effectively stabilize manganese atoms, could serve as the impetus for particle fragmentation and subsequent anchoring of isolated manganese species, leading to redispersion. However, extensive experimental validation of the proposed mechanism would be required and remains a subject for a separate, dedicated investigation.

2.6. Catalyst Design Guidelines

The main elements that distinguish Mn/CeO_2 as a remarkable catalytic material are summarized in **Figure 8**. At the foundation of its design lies the ability of CeO_2 to stabilize isolated atoms of manganese, as demonstrated by the combination of microscopy and EPR analyses. These can be formed by simple impregnation, using a small amount of metal (1 wt%). While CeO_2 is known as a support for single-atom catalysts,^[28,67] to our knowledge there have not been previous reports of surface-stabilized manganese. Indeed, the anchoring sites of the carrier appear to be sufficiently strong to prevent agglomeration during the reaction, resulting in a robust metal nanostructure and stable catalytic performance. The surface nature of the manganese species also allows them to remain in a low-valent, undercoordinated state, which in turn translates into the exceptional ability to activate gas-phase O_2 and facilitate N–N bond formation, as shown by the kinetic analysis and DFT modeling. This complements the inherent oxygen transfer ability of the support and enables the attainment of high N_2O selectivity and activity. Additionally, we found the active oxygen species to originate from the lattice of CeO_2 , while O_2 in the feed appears to primarily replenish their reserves. The involvement of lattice oxygen in both the initial dehydrogenation of NH_3 and the ulti-

mate formation of N_2O has been demonstrated by TAP experiments. Furthermore, the DFT simulations show cerium atoms adjacent to the isolated manganese sites to participate in stabilization of dehydrogenated NH_x intermediates, emphasizing the multifaceted role of CeO_2 . With this, we have gained both practical and fundamental insights into the structure and function of Mn/CeO_2 , revealing a novel class of CeO_2 -supported atomically-dispersed transition metal-based catalysts for N_2O formation via NH_3 oxidation. In fact, the combination of properties pertaining to the generation and supply of active oxygen species, which emerge as a result of the catalyst's unique nanostructure, are of relevance to selective catalytic oxidations in general and encourage future investigations for a range of other applications.

3. Conclusion

In summary, low-valent manganese atoms stabilized on CeO_2 are revealed as the first stable catalyst for NH_3 oxidation to N_2O , rivaling state-of-the-art Au/CeO_2 in terms of selectivity and reaching a two-fold higher N_2O productivity. The isolated manganese sites are primarily generated during synthesis via a simple impregnation, while in situ redispersion of few scattered MnO particles results in full atomic dispersion. The resultant material shows no structural changes or loss of catalytic activity over 70 h on stream. The oxygen transfer ability of CeO_2 is unveiled to be a fundamental property which promotes N_2O selectivity, setting CeO_2 apart from other redox-inactive carriers. Furthermore, the reaction is found to proceed with the direct participation of lattice oxygen of CeO_2 . Accordingly, low-valent manganese sites effectively activate gas-phase O_2 , thereby healing the vacancies and allowing the abundant supply of active oxygen species to be maintained. Furthermore, the isolated manganese species can facilitate the N–N bond formation between HNO intermediates via a cyclic intermediate closely related to NOR enzymes, ultimately leading to selective evolution of N_2O . The adjacent Ce atoms, in turn, aid in stabilizing dehydrogenated NH_x intermediates. This work sets an important milestone in the design and understanding of catalysts for NH_3 oxidation to N_2O , establishing CeO_2 -supported SACs as a highly promising class of materials for this application, as well as a range of other selective oxidation reactions.

4. Experimental Section

Catalyst Synthesis: Supported metal catalysts were synthesized by an IWI method. Metal precursors were dissolved in deionized water and the obtained solutions were added dropwise to the support. After impregnation, the samples were dried under vacuum at 353 K overnight and then calcined in static air at 673 or 823 K (heating rate = 3 K min^{-1} , hold time = 5 h). Au/CeO_2 was prepared by deposition precipitation with urea method, following the protocol described elsewhere.^[12] Additional details of the catalyst synthesis are provided in the Supporting Information.

Catalyst Characterization: Numerous techniques were employed to characterize the catalysts in fresh form and after use in NH_3 oxidation. Namely, the composition of the catalyst, metal speciation and dispersion were determined by X-ray fluorescence (XRF), XPS, EPR, H_2 -TPR, and HAADF-STEM. The specific surface area was determined by N_2 sorption

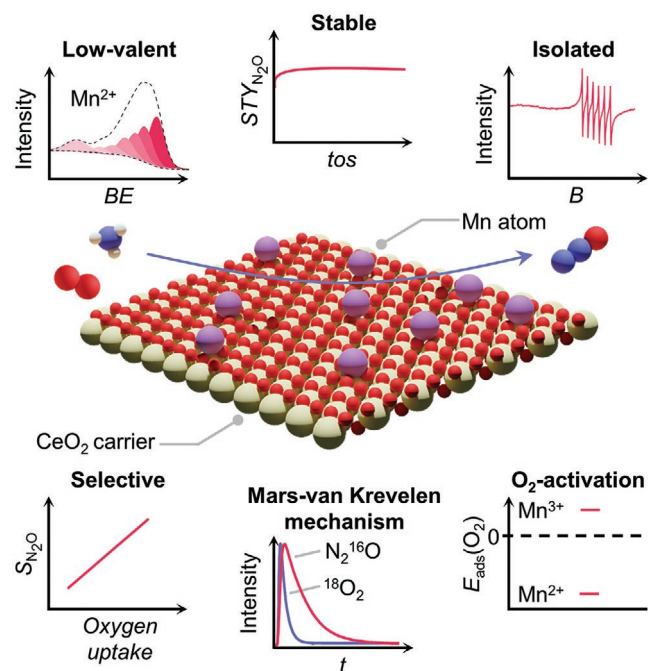


Figure 8. Summary of the key structural and catalytic properties of Mn/CeO_2 .

at 77 K. The interactions of the catalysts with O₂ were studied by static volumetric O₂ chemisorption at the reaction temperature (673 K). Details of all characterization techniques and procedures are provided in the Supporting Information.

Catalyst Evaluation: Evaluation of catalytic performance in continuous-flow NH₃ oxidation was conducted in a fixed-bed reactor set-up (depicted in Figure S1, Supporting Information and further described in the Supporting Information). In a typical test, the catalyst (particle size 0.15–0.4 mm, $m_{\text{cat}} = 0.004\text{--}0.5$ g for catalytic activity tests, and 0.04 g for kinetic and stability tests; for tests at elevated GHSV (> 32 000 cm³ h^{−1} g_{cat}^{−1}) the catalyst bed was diluted with SiC (particle size 0.5–0.6 mm) to avoid the formation of hot spots) was loaded into a quartz micro-reactor and activated in a He flow ($T_{\text{bed}} = 473$ K, $F_T = 40$ cm³ min^{−1}) for 30 min prior to the measurement. Subsequently, the reactor was heated to the desired temperature ($T_{\text{bed}} = 473\text{--}723$ K) and allowed to stabilize for at least 30 min before the reaction mixture (8 vol% NH₃, 8 vol% O₂, 4 vol% Ar, 80 vol% He) was fed at a total volumetric flow of $F_T = 16\text{--}250$ cm³ min^{−1}. The relevant performance metrics, including the NH₃ conversion, product selectivities, material balances, and criteria for the presence of mass and heat transfer limitations were quantified according to the protocols detailed in the Supporting Information.

Transient Mechanistic Studies: NH₃ oxidation was investigated in the temporal analysis of products (TAP-2) reactor operating in pulse mode. The catalyst (≈ 70 mg, particle size 0.2–0.4 mm) was packed between two layers of quartz particles (particle size 0.25–0.35 mm) in the isothermal zone of an in-house developed quartz reactor. After the exposure of the reactor to ≈ 10^{−5} Pa, ¹⁸O₂:NH₃:He = 1:1:1 mixture was pulsed (pulse size = 1.5 × 10¹⁵–5 × 10¹⁶ molecules) in the temperature range of 473–773 K with a 100 K step. The pulses were repeated ten times and averaged to improve the signal-to-noise ratio. The feed components and the reaction products were quantified by an online quadrupole mass spectrometer with a time resolution of ≈ 100 μs. The contribution of the compounds to the respective m/z values was estimated using standard fragmentation patterns determined in separate experiments. Additional details are provided in the Supporting Information.

Computational Details: To gain insights into the possible structural configurations of isolated manganese atoms on different surfaces of CeO₂, and their corresponding reactivity, DFT modelling was conducted with the Vienna Ab Initio Simulation Package (VASP 5.4.4),^[68] using the PBE functional,^[50] and the HSE03 hybrid functional with 13% exact exchange (HSE03-13).^[50,69] The valence electrons were extended in plane waves with a basis set cutoff of 500 eV.^[70,71] PBE+U framework was employed to carry out the structural relaxations. For cerium atoms, an additional Hubbard U term ($U_{\text{eff}} = 4.5$ V) was applied, following previous literature reports.^[52,72,73] Projector Augmented Wave (PAW) method was applied to the core electron, utilizing appropriate PAW–PBE pseudopotentials. Simulations were performed spin unrestricted, applying dipole corrections, where appropriate. The threshold for electronic convergence was set at 1 × 10^{−6} eV and the positions of atoms were relaxed until residual forces reached 0.015 eV Å^{−1}. For selected structures, HSE03-13 hybrid functional was also used to refine the energies, fixing the atomic coordinates at the PBE+U optimized positions. In view of the significantly higher computational cost of HSE03-13, the threshold for electronic convergence was lowered to 1 × 10^{−4} eV. Total energies of slab models were evaluated at the Gamma point throughout. Relative XPS shifts (core level binding energies) were calculated in the final state approximation^[74] and referenced to manganese in a 29-atom supercell of α-Mn. The code developed by Henkelman et al. was used for Bader charge analysis.^[75–78]

For the (111), (110), and (100) facets of CeO₂ slab models were constructed as (3 × 3), (2 × 2), and (3 × 3) supercells, extending 9, 6, and 9 atomic layers along the z -direction, of which the bottom 4, 3, and 4 layers were fixed at the optimized bulk positions, respectively. At least 10 Å of vacuum was added on top of the surfaces to minimize interactions of vertically repeated slab images under periodic boundary conditions. Formal oxidation states of manganese single-atoms were assigned using the localized magnetic moments of reduced Ce³⁺ centers, where a threshold of 0.8 μ_B was applied.^[48] Single-atom manganese adsorption

and substitution energies were calculated following Equations (8) and (9), where $E_{\text{SAC}}^{\text{ads}}$ and $E_{\text{SAC}}^{\text{sub}}$ are the energies of the respective single-atom catalysts (SACs), E_{pris} is the energy of the corresponding pristine ceria slab, E_{Mn} is the energy of single-atom manganese, using α-Mn as reference ($E_{\text{coh}} = -8.98$ eV atom^{−1}), and E_{Ce} is the energy of the substituted cerium atom, evaluated via Equation (10). Adsorption energies of reactants and reaction intermediates were evaluated using Equation (8), accordingly.

$$E_{\text{ads}} = E_{\text{SAC}}^{\text{ads}} - E_{\text{pris}} - E_{\text{Mn}} \quad (8)$$

$$E_{\text{sub}} = E_{\text{SAC}}^{\text{sub}} - E_{\text{pris}} - E_{\text{Mn}} + E_{\text{Ce}} \quad (9)$$

$$E_{\text{Ce}} = E_{\text{CeO}_2} - E_{\text{O}_2} \quad (10)$$

Statistical Analysis: All catalytic data (i.e., conversion, selectivity, STY) are presented as arithmetic mean ± 95% confidence interval, based on at least two repeated measurements under the specified conditions. Source data obtained from selected characterization techniques (i.e., H₂-TPR, XRD, EPR) were plotted as received without further manipulation. O₂ chemisorption values (i.e., oxygen uptake) were acquired based on Sinfelt analysis method of the corresponding isotherms, performed on the 3Flex software (V 5.01, Micromeritics Instrument Corp., US). Specific surface area values were acquired based on Brunauer–Emmett–Teller analysis method, performed on TriStar II 3020 software (V 3.02, Micromeritics Instrument Corp., US). Metal content based on XRF analysis was determined using the built-in quantitative analysis tool of ORBIS Vision software (V 2.148, EDAX Inc. US). The particle size distribution presented in Figure S4 and S10 were determined through analysis of > 100 particles identified on the HAADF-STEM micrographs and elemental mappings, using ImageJ software (V 1.52a, National Institute of Health, US). The corresponding plots were created using OriginPro 2019 software (V 9.6.0.172, OriginLab Corp., US), assuming a normal distribution of particle size. XPS spectra were subject to charge correction based on the C 1s photoemission of adventitious carbon, set at 284.8 eV, prior to the fitting. The fitting was performed using CasaXPS software (V 2.3.23PR1.0, Casa Software Ltd., UK), as described in the respective section of the Supporting Information.

Supporting Information

Supporting Information is available from the Wiley Online Library or from the author.

Acknowledgements

I.S. and Z.T. contributed equally to this work. This publication was created as part of NCCR Catalysis (180544), a National Centre of Competence in Research funded by the Swiss National Science Foundation. R.E. and H.E. acknowledge the financial support by the Swiss National Science Foundation (project No. 200021_196381). Electron microscopy was done at the Scientific Center for Optical and Electron Microscopy (ScopeM) of the ETH Zurich and the Electron Microscopy Center of EMPA. The work of J.G. and N.L. was funded by the Generalitat de Catalunya and the European Union under Grant 2020_FI_B 00266, the Ministry of Science and Innovation (PID2021-122516OB-I00, MCIN/AEI/10.13039/501100011033, CEX2019-000925-S). The Barcelona Supercomputing Center (BSC-RES) is acknowledged for providing generous computational resources.

Open access funding provided by Eidgenössische Technische Hochschule Zurich.

Conflict of Interest

The authors declare no conflict of interest.

Data Availability Statement

The data that support the findings of this study are openly available in Zenodo at <https://doi.org/10.5281/zenodo.7380563>, reference number 7380563, and ioChem-BD at <http://dx.doi.org/10.19061/iochem-bd-1-262>.

Keywords

ammonia oxidation, ceria, manganese, nitrous oxide, single-atom catalysis

Received: December 2, 2022

Revised: February 17, 2023

Published online: May 1, 2023

- [1] Z. Guo, B. Liu, Q. Zhang, W. Deng, Y. Wang, Y. Yang, *Chem. Soc. Rev.* **2014**, 43, 3480.
- [2] I. Hermans, E. S. Spier, U. Neuenschwander, N. Turrà, A. Baiker, *Top. Catal.* **2009**, 52, 1162.
- [3] J. Pérez-Ramírez, C. Mondelli, T. Schmidt, O. F. K. Schlüter, A. Wolf, L. Mleczko, T. Dreier, *Energy Environ. Sci.* **2011**, 4, 4786.
- [4] F. Cavani, *Catal. Today* **2010**, 8, 157.
- [5] S. Siankevich, G. Savoglids, Z. Fei, G. Laurenczy, D. T. L. Alexander, N. Yan, P. J. Dyson, *J. Catal.* **2014**, 315, 67.
- [6] V. N. Parmon, G. I. Panov, A. Uriarte, A. S. Noskov, *Catal. Today* **2005**, 100, 115.
- [7] A. K. Uriarte, *Stud. Surf. Sci. Catal.* **2000**, 130, 743.
- [8] G. I. Panov, K. A. Dubkov, A. S. Kharitonov, in *Modern Heterogeneous Oxidation Catalysis* (Ed: N. Mizuno), Wiley VCH, Hoboken, NJ **2009**.
- [9] L. V. Pirutko, V. S. Chernyavsky, A. K. Uriarte, G. I. Panov, *Appl. Catal. A Gen.* **2002**, 227, 143.
- [10] M. V. Parfenov, E. V. Starokon, L. V. Pirutko, G. I. Panov, *J. Catal.* **2014**, 318, 14.
- [11] Office of Air Quality Planning and Standards, *AP42 Background Report. Adipic Acid Production*, U. S. Environmental Protection Agency, Research Triangle Park, NC, **1997**.
- [12] Z. Tang, I. Surin, A. Rasmussen, F. Krumeich, E. V. Kondratenko, V. A. Kondratenko, J. Pérez-Ramírez, *Angew. Chem., Int. Ed.* **2022**, 61, e202200772.
- [13] Grand View Research, Nitrous Oxide Market Size & Share, Global Industry Report, 2018-2025, [grandviewresearch.com/industry-analysis/nitrous-oxide-market](https://www.grandviewresearch.com/industry-analysis/nitrous-oxide-market), accessed: September, 2022.
- [14] J. Pérez-Ramírez, E. V. Kondratenko, V. A. Kondratenko, M. Baerns, *J. Catal.* **2004**, 227, 90.
- [15] V. A. Sadykov, L. A. Isupova, I. A. Zolotarskii, L. N. Bobrova, A. S. Noskov, V. N. Parmon, E. A. Brushtein, T. V. Telyatnikova, V. I. Chernyshev, V. V. Lunin, *Appl. Catal. A Gen.* **2000**, 204, 59.
- [16] S. Ghavam, M. Vahdati, I. A. G. Wilson, P. Styring, *Front. Energy Res.* **2021**, 9, 580808.
- [17] C. Smith, A. K. Hill, L. Torrente-Murciano, *Energy Environ. Sci.* **2020**, 13, 331.
- [18] C. D. Chang, S. A. Stevenson, J. C. Vartuli (ExxonMobil Oil Corporation US), USOO6312657B1, **2001**.
- [19] N. Ilchenko, *J. Catal.* **1975**, 39, 73.
- [20] K. Fujiwara, H. Kato, K. Wakimura, H. Nakamura, S. Yoshinaga (Mitsui Toatsu Chemicals Inc. JP), EP0799792A1, **1997**.
- [21] J. Ludvíková, M. Jablonská, K. Jirátková, L. Chmielarz, J. Balabánová, F. Kovanda, L. Obalová, *Res. Chem. Intermed.* **2016**, 42, 2669.
- [22] V. V. Mokhrinskii, E. M. Slavinskaya, A. S. Noskov, I. A. Zolotarskii (SOLUTIA Inc. US), WO98/25698, **1998**.
- [23] A. S. Ivanova, E. M. Slavinskaya, V. V. Mokhrinskii, I. A. Polukhina, S. V. Tsybulya, I. P. Prosvirin, V. I. Bukhtiyarov, V. A. Rogov, V. I. Zaikovskii, A. S. Noskov, *J. Catal.* **2004**, 221, 213.
- [24] E. M. Slavinskaya, S. A. Veniaminov, P. Notté, A. S. Ivanova, A. I. Boronin, Y. A. Chesalov, I. A. Polukhina, A. S. Noskov, *J. Catal.* **2004**, 222, 129.
- [25] A. Wollner, F. Lange, H. Schmelz, H. Knozinger, *Appl. Catal. A Gen.* **1993**, 94, 181.
- [26] S. Hinokuma, H. Shimanoe, Y. Kawabata, S. Kiritoshi, K. Araki, M. Machida, *Catal. Commun.* **2018**, 105, 48.
- [27] J. Petryk, E. Kołakowska, *Appl. Catal. B* **2000**, 24, 121.
- [28] R. Lang, X. Du, Y. Huang, X. Jiang, Q. Zhang, Y. Guo, K. Liu, B. Qiao, A. Wang, T. Zhang, *Chem. Rev.* **2020**, 120, 11986.
- [29] S. K. Kaiser, Z. Chen, D. Faust Akl, S. Mitchell, J. Pérez-Ramírez, *Chem. Rev.* **2020**, 120, 11703.
- [30] S. Mitchell, R. Qin, N. Zheng, J. Pérez-Ramírez, *Nat. Nanotechnol.* **2021**, 16, 129.
- [31] F. Kapteijn, A. D. Vanlangeveld, J. A. Moulijn, A. Andreini, M. A. Vuurman, A. M. Turek, J. M. Jehng, I. E. Wachs, *J. Catal.* **1994**, 150, 94.
- [32] A. Trovarelli, *Catal. Rev. Sci. Eng.* **1996**, 38, 439.
- [33] H. Wang, J. X. Liu, L. F. Allard, S. Lee, J. Liu, H. Li, J. Wang, J. Wang, S. H. Oh, W. Li, M. Flytzani-Stephanopoulos, M. Shen, B. R. Goldsmith, M. Yang, *Nat. Commun.* **2019**, 10, 3808.
- [34] K. Ma, W. Liao, W. Shi, F. Xu, Y. Zhou, C. Tang, J. Lu, W. Shen, Z. Zhang, *J. Catal.* **2022**, 407, 104.
- [35] A. Sultana, M. Sasaki, H. Hamada, *Catal. Today* **2012**, 185, 284.
- [36] S. Imamura, M. Shono, N. Okamoto, A. Hamada, S. Ishida, *Appl. Catal. A Gen.* **1996**, 142, 279.
- [37] E. S. Ilton, J. E. Post, P. J. Heaney, F. T. Ling, S. N. Kerisit, *Appl. Surf. Sci.* **2016**, 366, 475.
- [38] A. S. Ivanova, E. M. Slavinskaya, V. V. Mokhrinskii, I. A. Polukhina, S. V. Tsybulya, I. P. Prosvirin, V. I. Bukhtiyarov, V. A. Rogov, V. I. Zaikovskii, A. S. Noskov, *J. Catal.* **2004**, 221, 213.
- [39] A. S. Noskov, I. A. Zolotarskii, S. A. Pokrovskaya, V. N. Korotkiikh, E. M. Slavinskaya, V. V. Mokhrinskii, V. N. Kashkin, *Chem. Eng. J.* **2003**, 91, 235.
- [40] L. D. Bogomolova, Y. G. Teplakov, F. Caccavale, *J. Non-Cryst. Solids* **1996**, 194, 291.
- [41] I. Ardelean, M. Flora, *J. Mater. Sci.: Mater. Electron.* **2002**, 13, 357.
- [42] J. Zawadzki, *Discuss. Faraday Soc.* **1950**, 8, 140.
- [43] K. Otto, M. Shelef, J. T. Kummer, *J. Phys. Chem.* **1970**, 74, 2690.
- [44] O. N. Sil'chenkova, V. N. Korchak, V. A. Matyshak, *Kinet. Catal.* **2002**, 43, 363.
- [45] E. M. Slavinskaya, Y. A. Chesalov, A. I. Boronin, I. A. Polukhina, A. S. Noskov, *Kinet. Catal.* **2005**, 46, 555.
- [46] M. Capdevila-Cortada, Z. Łodziana, N. López, *ACS Catal.* **2016**, 6, 8370.
- [47] A. Walsh, A. A. Sokol, J. Buckeridge, D. O. Scanlon, C. R. A. Catlow, *Nat. Mater.* **2018**, 17, 958.
- [48] N. Daelman, M. Capdevila-Cortada, N. Lopez, *Nat. Mater.* **2019**, 18, 1215.
- [49] J. Geiger, N. López, *J. Phys. Chem. C* **2022**, 126, 13698.
- [50] J. P. Perdew, K. Burke, M. Ernzerhof, *Phys. Rev. Lett.* **1996**, 77, 3865.
- [51] J. Hubbard, *Proc. Math. Phys. Eng. Sci.* **1963**, 276, 238.
- [52] S. L. Dudarev, G. A. Botton, S. Y. Savrasov, C. J. Humphreys, A. P. Sutton, *Phys. Rev. B* **1998**, 57, 1505.
- [53] F. S. Hegner, D. Cardenas-Morcoso, S. Gimenez, N. López, J. R. Galan-Mascaros, *ChemSusChem* **2017**, 10, 4552.
- [54] T. Hino, Y. Matsumoto, S. Nagano, H. Sugimoto, Y. Fukumori, T. Murata, S. Iwata, Y. Shiro, *Science* **2010**, 330, 1666.
- [55] E. Ferretti, S. Dechert, S. Demeshko, M. C. Holthausen, F. Meyer, *Angew. Chem. Int. Ed. Engl.* **2019**, 58, 1705.
- [56] A. M. Wright, T. W. Hayton, *Inorg. Chem.* **2015**, 54, 9330.
- [57] J. Jover, C. K. Brozek, M. Dincă, N. López, *Chem. Mater.* **2019**, 31, 8875.
- [58] F. Schreiber, P. Wunderlin, K. M. Udert, G. F. Wells, *Front. Microbiol.* **2012**, 3, 372.
- [59] C. Fehling, G. Friedrichs, *J. Am. Chem. Soc.* **2011**, 133, 17912.

- [60] J. Pérez-Ramírez, E. V. Kondratenko, *Catal. Today* **2007**, 121, 160.
- [61] K. Morgan, N. Maguire, R. Fushimi, J. T. Gleaves, A. Goguet, M. P. Harold, E. V. Kondratenko, U. Menon, Y. Schuurman, G. S. Yablonsky, *Catal. Sci. Technol.* **2017**, 7, 2416.
- [62] D. Wang, Q. Yao, C. Mou, S. Hui, Y. Niu, *Fuel* **2019**, 254, 115719.
- [63] L. Nie, D. Mei, H. Xiong, B. Peng, Z. Ren, X. I. Pereira-Hernandez, A. DeLaRiva, M. Wang, M. H. Engelhard, L. Kovarik, A. K. Datye, Y. Wang, *Science* **2017**, 358, 1419.
- [64] E. J. Peterson, A. T. DeLaRiva, S. Lin, R. S. Johnson, H. Guo, J. T. Miller, J. Hun Kwak, C. H. Peden, B. Kiefer, L. F. Allard, F. H. Ribeiro, A. K. Datye, *Nat. Commun.* **2014**, 5, 4885.
- [65] V. Giulimondi, S. K. Kaiser, M. Agrachev, F. Krumeich, A. H. Clark, S. Mitchell, G. Jeschke, J. Pérez-Ramírez, *J. Mater. Chem. A* **2022**, 10, 5953.
- [66] K. Morgan, A. Goguet, C. Hardacre, *ACS Catal.* **2015**, 5, 3430.
- [67] J. Jones, H. Xiong, A. T. DeLaRiva, E. J. Peterson, H. Pham, S. R. Challa, G. Qi, S. Oh, M. H. Wiebenga, X. I. Pereira-Hernandez, Y. Wang, A. K. Datye, *Science* **2016**, 353, 150.
- [68] G. Kresse, J. Furthmüller, *Comput. Mater. Sci.* **1996**, 6, 15.
- [69] F. S. Hegner, I. Herraiz-Cardona, D. Cardenas-Morcoso, N. López, J. R. Galan-Mascaros, S. Gimenez, *ACS Appl. Mater. Interfaces* **2017**, 9, 37671.
- [70] G. Kresse, D. Joubert, *Phys. Rev. B* **1999**, 59, 1758.
- [71] P. E. Blochl, *Phys. Rev. B* **1994**, 50, 17953.
- [72] J. Hubbard, *Proc. Math. Phys. Eng. Sci.* **1997**, 276, 238.
- [73] S. Fabris, S. de Gironcoli, S. Baroni, G. Vicario, G. Balducci, *Phys. Rev. B* **2005**, 71, 041102.
- [74] N. Pueyo Bellafont, F. Vines, W. Hieringer, F. Illas, *J. Comput. Chem.* **2017**, 38, 518.
- [75] W. Tang, E. Sanville, G. Henkelman, *J. Phys. Condens. Matter* **2009**, 21, 084204.
- [76] E. Sanville, S. D. Kenny, R. Smith, G. Henkelman, *J. Comput. Chem.* **2007**, 28, 899.
- [77] G. Henkelman, A. Arnaldsson, H. Jónsson, *Comput. Mater. Sci.* **2006**, 36, 354.
- [78] M. Yu, D. R. Trinkle, *J. Chem. Phys.* **2011**, 134, 064111.
- [79] M. Alvarez-Moreno, C. de Graaf, N. López, F. Maseras, J. M. Poblet, C. Bo, *J. Chem. Inf. Model.* **2015**, 55, 95.